2024 IEEE International Conference on Robotics and Automation (ICRA 2024)
May 13-17, 2024. Yokohama, Japan

Towards Centimeter-Scale Underwater Mobile Robots: An Architecture for Capable μAUVs

Pascal Spino[1,2] and Daniela Rus[2]

***Abstract*— Underwater robots are indispensable for aquatic exploration, yet their size and complexity often limit broader application. This research presents a pioneering micro autonomous underwater vehicle (μAUV) design. This robot is distinguished by its utilization of mass-produced drone components, novel jet propulsion mechanisms, and multifunctional spherical shell. Its architecture is modular, appendage-free, and largely seal-free. Preliminary tests highlight its motion capabilities and set new benchmarks for centimeter-scale μAUV advancements.**

I. Introduction

Autonomous underwater vehicles (AUVs) play an increasingly important role in Earth's many aquatic environments. Applications include search and rescue missions, infrastructure inspection, ecosystem monitoring, and deep ocean surveys. AUVs have the capability of performing dangerous tasks with greater accuracy and endurance than humans [1] and are on a trend of increasing research focus [2]. However, the underwater environment remains a challenging medium for robotic development. Most systems tend to be large and complex, making them unsuitable for many domains as well as prohibitively expensive to build, deploy, and maintain. There is much interest in developing new classes of micro autonomous underwater vehicles (μAUVs) that offer similar capabilities to AUV but in much smaller packages [3] [4] [5]. μAUV are also particularly attractive for the emerging potential to be deployed in large swarms [6].

This work describes and validates a novel architecture of extremely small μAUV. The spherical robot shown in Fig. 1 measures $64\,\mathrm{mm}$ in diameter with a dry mass of $120\,\mathrm{g}$. This makes it the smallest of all comparable μAUV systems in literature to be capable of controlled three-dimensional motion. The robot additionally utilizes a novel jet-based propulsion system that sets new benchmarks for swimming efficiency and speed among machines at the centimeter scale. The architecture can feasibly scale larger or smaller and the present size is motivated by the availability of low-cost and off-the-shelf hardware. In small quantities the robot costs less than $\$200$ excluding tooling and can be manufactured in a few hours by commercial 3D printers and limited manual assembly. The robot is demonstrated to be manoeuvrable, resilient to collisions, and relatively high endurance. It presents opportunities for exploration of shipwrecks and caves, for low-disturbance observation of marine ecosystems, and for research in swarm robotics.

[1]Department of Mechanical Engineering, Massachusetts Institute of Technology, Cambridge, MA, 02139, USA spino@mit.edu
[2]Computer Science and Artificial Intelligence Laboratory, Massachusetts Institute of Technology, Cambridge, MA, 02139, USA

Fig. 1. The assembled robot ($64\,\mathrm{mm}$) beside a baseball ($73\,\mathrm{mm}$) for scale.

This paper makes the following contributions:

- Design and fabrication of a compact μAUV with novel jet-based actuators
- Characterization of the μAUV and its propulsion system, and validation of its motion capabilities

II. Related Work

Spherical underwater robots have received ongoing interest for applications involving confined-space exploration and deep submergence. Early work in spherical μAUV can be found here [7] [8] [9]. Some groups have developed spherical μAUV at the $\sim 100\,\mathrm{mm}$ scale for in-pipe inspection [10] [11]. Sphere-like μAUV most commonly use internal pumps and fluid jet systems that exhibit good propulsive forces, but with poor or unreported efficiencies and via complex actuation mechanisms. Modern AUV that operate in deep oceans also use spherical pressure vessels [12], but are much larger and non-spherical overall, and otherwise dissimilar in design.

Another related class of robot are fish-like μAUV, which are shaped to resemble their natural counterparts and most commonly utilize flapping mechanisms for propulsion. Examples have been demonstrated on the scale of $100\,\mathrm{mm}$ to $400\,\mathrm{mm}$ in terms of longest dimension [13] [14] [15]. Matured work includes the CoCoRo and BlueSwarm projects, which produced the Jeff unit at the scale of $250\,\mathrm{mm}$ [16] and BlueSwarm unit at the scale of $130\,\mathrm{mm}$ [17] [6], respectively. This class of μAUV has been explored as swarm and biomimetic research platforms but generally report low propulsive forces and are mechanically complex.

Other underwater robots that operate at a similar scale include passive vehicles that drift with ocean currents [18], soft hydraulic robots [19], and insect-scale swimming robots [20] [21]. These platforms are not considered direct comparisons to μAUV due to insufficient motion capabilities or lack of mass capacity for onboard energy and actuation.

979-8-3503-8457-4/24/$31.00 ©2024 IEEE

III. Design

A. Mechanical Design

Fig. 2 provides an overview of the robot structure and propulsive degrees of freedom (DOF). Table I summarizes its capabilities. Beneficial design paradigms are highlighted in this section and described in greater detail in later sections:

The shell serves many purposes: The spherical shell is produced primarily from a single material and process, and acts in parts structurally, in parts as a pressure vessel, and in parts as a vectoring device for the propulsion system. Nearly half of the robot's mass is associated with the shell alone, which is assembled from a several parts to outwardly form a sphere with one forward-facing window. A spherical exterior is selected for relatively low drag in multidirectional translation as well as other useful benefits like pressure tolerance, collision resilience, and low inertial and drag resistance to rotation for maneuverability. Built into the internal structure of the shell is a large resealable watertight enclosure and four peripheral flooded segments – one for each thrust actuator. The structural elements of the actuators, which include impeller mounting fixtures, volutes, and jet nozzles are built directly into the geometry of the shell. Advancements in resin 3D printing allow this complex component to be manufactured at low-cost.

The actuators are mechanically simple: The propulsion system operates by generating four fluid jets at fixed orientations and variable flow rates via embedded centrifugal impellers. This approach leverages simple actuators that are free of both appendages and seals. The electromechanical components are confined within the shell as opposed to the more conventional propeller devices used by larger AUV; this internal arrangement protects the delicate elements. The actuator incorporates a novel configuration of magnetic couplings to transfer torque between motor and impeller stages without the need for seals. The propulsion configuration presented in this work provides the robot with control authority over forward translation, diving translation, yaw rotation, and roll rotation through jet combinations. The jet mechanisms cannot be driven in reverse and so the actuators only provide unidirectional thrust. Excluding control hardware and fasteners, each actuator is assembled from five unique components that are each either commercially available or 3D printed.

The hardware is densely packed: A modular electromechanical assembly that contains all components for computation, sensing, actuation, and energy storage is protected in a watertight enclosure within the shell. The assembly, which is shown in Fig. 3, is held in place by passive alignment features in the shell and is completely removable by unfastening the lid of the shell and lifting upwards. This modular approach is beneficial for maintenance, as all elements of the robot can be easily accessed and the shell can be replaced in case of corrosion or damage. The assembly is arranged to position heavier components like the motors and battery as low as possible in the robot, which provides passive pitch and roll stability. The actuator design allows for efficient packing that fills the internal volume of the shell.

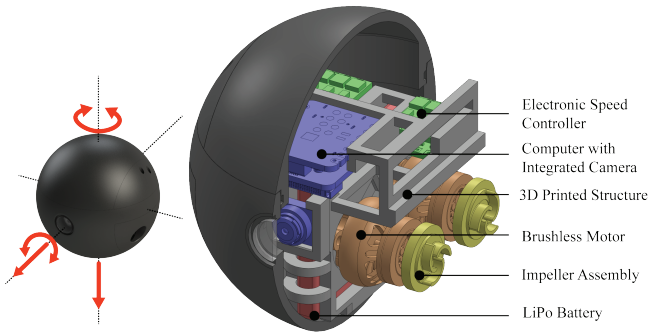

Fig. 2. Isometric view of the robot with red arrows indicating its four actuated degrees of freedom (left) and an enlarged view with half of the shell removed to reveal major internal components (right).

TABLE I
Robot Characteristics and Features

Size	64 mm, spherical
Mass	120 g (+15 g payload)
DOF	250 mm/s forward translation 200 mm/s diving translation 360 °/s yaw rate
Endurance	$\leq$ 120 mins low thrust $\leq$ 25 mins high thrust
Camera	1600 × 1200 resolution
Cost	$180

B. Electronics

The scale of this μAUV is enabled in part by advancements in small aerial drone components. The thrust actuators are produced from 5000 KV brushless motors manufactured for 3-inch quadroters, and are driven by 1 S microelectronic speed controllers (ESC's). The robot's computer is a XIAO microcontroller unit built from a dual-core ESP32S3 with an integrated OV260 camera sensor. This camera system is suitable for computer-vision applications. The microcontroller also contains BlueTooth connectivity and microSD storage for recording images and videos. The onboard battery is a 500 mAh 1 S LiPo cell. The robot contains 15 g of mass capacity while maintaining positive buoyancy, which is more than enough to double its battery storage (currently 10 g) and include additional sensors depending on application. The next versions of this robot will include BMI270 inertial and MS5827 pressure sensors, which add insignificant mass.

C. Manufacturing

The robot's shell is fabricated in six pieces by a Carbon M1 3D printer in UMA90 resin as shown by Fig. 4. The two largest pieces are designed to interface with an O-ring in a radial configuration to produce the resealable watertight enclosure. Fasteners are embedded in the printed structure for assembly and disassembly. The watertight enclosure has a constant wall thickness of 2 mm except for the actuation points, where the enclosure wall is 1.5 mm thick. No post-processing is necessary for waterproofing, but the maximum

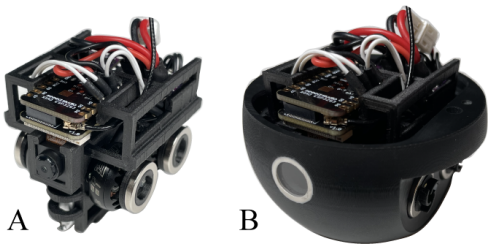

Fig. 3. (**A**) Internal robotic module containing densely packed controller, camera, ESCs, motors, and battery. (**B**) The same module as in before, but set into a partially assembled shell. The camera is centered at the window.

depth for which the shell can withstand has not been experimentally validated; extended submersion at $\leq 1\,\mathrm{m}$ depths and many underwater collisions have produced no leaks. The impeller blades are produced by the same material and process. The structural components within the shell's watertight enclosure are manufactured by a standard 3D printer. The circular window is laser cut from acrylic, press-fit into the shell, and sealed with marine epoxy.

IV. Jet Propulsion System

Swimming by jet propulsion presents opportunities at the centimeter scale that have not been comprehensively explored. A major limitation for fluid jet propulsion has been its inherent inefficiency; propulsion devices that move large fluid volumes with low acceleration require less energy than those that move low fluid volumes at high acceleration for identical thrusts [22] [23]. However, despite presenting an apparent energetic disadvantage, jet propulsion is a common swimming mechanism in nature and particularly prevalent among centimeter-scale animals like salp [24], squid [25], and nautilus [26]. Propulsion by fluid jets may provide significant benefits at certain scales that counteract its relatively high energetic cost; for example, benefits in maneuverability or overall drag reduction. The actuation system developed for this robot is suitable for further investigation of fluid jet propulsion as an enabling technology for μAUV.

A. Actuator

The robot has four identical and independently controllable actuators situated in its lower hemisphere. The combined actuator mass accounts for about one-third of the robot's total mass. The thrust forces produced are dominated by the orientation at which the fluid jets exit the shell and not the location of the actuator mechanisms themselves, which provides some design freedom with respect to their location on the robot. Each actuator weighs less than $10\,\mathrm{g}$ and consists of two stages: (1) a brushless motor with ESC, and (2) an impeller pump system enclosed by channels in the shell. An exploded view of the actuator is provided by Fig. 5 and the physical system is also pictured as part of the assembly in Fig. 3. The first stage converts onboard electrical energy to mechanical rotation and is housed entirely within the watertight enclosure of the robot. The second stage is flooded with water and converts rotation to fluid jets in fixed thrust vectors. The two stages are magnetically coupled.

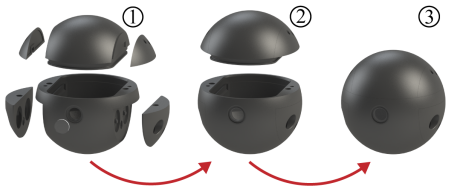

Fig. 4. Assembly process of the six resin-3D printed parts that form the spherical shell of the robot. The two bodies in step (2) interface with an O-ring to form the resealable watertight enclosure.

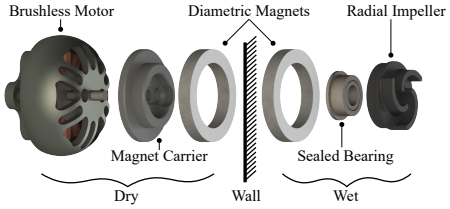

Fig. 5. Exploded view of the thrust actuator. Half of the assembly is protected within the watertight enclosure and the other half is exposed to water. The two halves are magnetically coupled across a thin wall.

B. Magnetic Coupling

It is difficult to pass rotational motion across a watertight enclosure boundary; the typical methods involve using a coupling shaft that penetrates the pressure vessel wall with a tight-fitting seal, or moving all motion stages outside of the enclosure. Both approaches negatively impact propulsive efficiency - the former because of friction at the shaft-seal interface, and the latter from hydrodynamic drag on machine elements. Both approaches are difficult to miniaturize and suffer from corrosion. In this robot, the internal motor stage instead drives the external impeller with a virtual shaft generated by magnetic forces that pass directly through the enclosure wall. This arrangement is known as a magnetic couple and has been successful in a variety of applications, including some thrust systems on existing underwater robots [16] [27]. This architecture departs from previous efforts in the extreme miniaturization and high density of magnetically coupled drives enabled by small changes to the mechanism. Magnetic couplings generally suffer from requiring complex fixtures and accommodating inherently low maximum torques relative to mechanism size and mass. Here, a single diametrically magnetized neodymium ring is used to concentrate magnetic mass in a large diameter, thin band. This geometry is advantageous to translate large torques relative to magnetic mass. Each stage of the actuator is supported to remain concentric and axially separated on ball bearings, which act against the attractive normal force developed between the coupling halves. The choice of a centrifugal impeller in combination with this form of magnetic coupling produces an inherently low-torque, mechanically simple, and small actuator - something prior approaches have not had the benefit of. This magnetic coupling arrangement is experimentally found to support a maximum torque of $\sim 2 \times 10^{-3}\,\mathrm{Nm}$ at a separation distance of $2.8\,\mathrm{mm}$.

C. Water Jets

Robot motion necessitates inducing fluid flow in the opposite direction of desired motion. The actuators create suction that draws in water from the sides of the robot and drive it along the millimeter-scale vectoring channels through the shell. The water exits the shell through nozzles at fixed points and orientations, and in doing so imparts thrust on the robot body. The water jets cannot be driven in reverse and so the actuator cannot produce bidirectional thrusts; jet orientations could be reconfigured to act antagonistically for reverse modes, or along different vectors to provide different DOF. Fig 6 shows the jet system in more detail with a cross section of the shell revealing internal channels. The robot maintains positive buoyancy for passive surfacing. Each actuator generates a pair of forces located at the centerlines of the channel inlet and outlet, respectively, due to flow occurring at both locations. Neglecting small pressure differences between the inlet and outlet, and assuming that the fluid velocity through the channel is much greater than freestream velocity, the magnitude of thrust developed by each actuator in steady state is equal to the rate of change of fluid momentum across the actuator channel:

$$\begin{bmatrix} F_{n,o} \\ F_{n,i} \end{bmatrix} = \begin{bmatrix} \dot{m}_n v_{n,o} \\ \dot{m}_n v_{n,i} \end{bmatrix} \quad \text{for} \quad n = 1, 2, 3, 4 \tag{1}$$

Where the outlet ($F_{n,o}$) and inlet ($F_{n,i}$) forces are aligned as shown in Fig. 6 and $v_{n,o}$ is the outlet fluid velocity, $v_{n,i}$ is the inlet fluid velocity, and $\dot{m}_n$ is the mass flow rate through the n^{th} actuator channel. The fluid (water) is incompressible and so the flow velocities at the inlet and outlet can be expressed in terms of channel cross-section area A_s, mass flow rate, and fluid density ρ:

$$v_{n,s} = \frac{\dot{m}_n}{\rho A_s} \quad \text{for} \quad s = i, o \tag{2}$$

It then follows that the forces developed by each actuator at the inlet and outlet are not independent and, for a given flow rate, are related in magnitude by the ratio of channel areas:

$$F_{n,i} = \frac{A_o}{A_i} F_{n,o} \tag{3}$$

For control purposes it is useful to derive the actuation control matrix, B, that describes the forces and moments produced on the robot body in terms of the outlet jet forces:

$$\begin{bmatrix} F_x & F_y & F_z & M_x & M_y & M_z \end{bmatrix}^T = B \begin{bmatrix} F_{1,o} \\ F_{2,o} \\ F_{3,o} \\ F_{4,o} \end{bmatrix} \tag{4}$$

Solving the free-body diagram shown in Fig 6 and applying the relationship in (3) yields:

$$B = \begin{bmatrix} 1 & 0 & 0 & 1 \\ 0 & 0 & 0 & 0 \\ 0 & -1 & -1 & 0 \\ 0 & -\alpha & \alpha & 0 \\ 0 & 0 & 0 & 0 \\ -\alpha & 0 & 0 & \alpha \end{bmatrix} + \frac{A_o}{A_i} \begin{bmatrix} 0 & 0 & 0 & 0 \\ 1 & 1 & -1 & -1 \\ 0 & 0 & 0 & 0 \\ \gamma & \gamma & -\gamma & -\gamma \\ 0 & 0 & 0 & 0 \\ -\beta & \beta & -\beta & \beta \end{bmatrix} \tag{5}$$

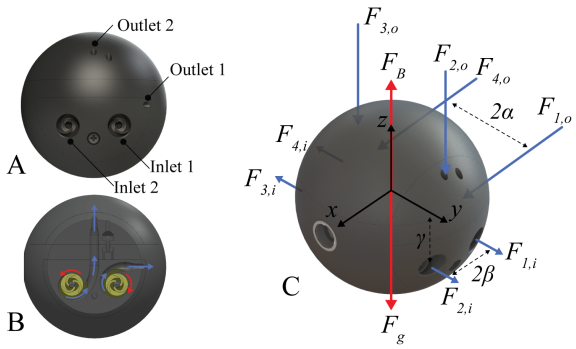

Fig. 6. (**A**) Side view of the robot, facing left, indicating where water enters and exits the shell for thrust generation; a mirrored arrangement is on the opposite side of the robot (**B**) Cross section with the same view as above, except showing the internal flooded structure. (**C**) Isometric free-body diagram showing thrust forces developed from jets, gravitational and buoyancy forces, and coordinate system convention. The inlet diameter is 9 mm, the outlet diameter is 2.5 mm, α=24 mm, β=10 mm, and γ=8 mm.

Here the actuation control matrix B is subdivided into a sum of two matrices; the matrix on the left represents the components due to outlet thrusts, and the matrix on the right represents the components due to inlet thrusts. The inlet area is much larger than the outlet area ($A_o/A_i = 0.08$), and so the outlet thrusts have a dominant effect. The robot DOF from Fig. 2 are also identifiable from the left matrix in (5). This analysis provides a basis for the inverse problem of designing jet positions and orientations that achieve desired motion characteristics.

V. Experiments

A. Test Setup

All experiments were performed in an aquarium tank significantly larger than the robot (0.48 m × 0.23 m). Custom equipment was developed to characterize the thrust generated and power consumed by the robot's propulsion system in a static case. The test hardware consisted of a TAL221 100 g load cell with HX711 amplifier to measure thrust force, ACS724 hall effect current sensor to measure power consumption, and a SAMD21 microcontroller for synchronizing and recording measurements at 2 Hz. A modified version of the robot shell was produced with fixtures and a powerline tether to interface with the test equipment. The robot was programmed to provide thrust in five percent increments of ESC throttle, with the maximum ESC throttle corresponding to the maximum speed at which the motors can be driven. ESC throttles below twenty percent are not shown because the actuators have a deadband in this range, which is common to small propulsion systems [28]. Thrust tests consisted of the robot providing equal thrust from both forward actuators for five seconds at each throttle increment with periods of rest in-between. The fixture that held the robot pivoted about bearings and was supported at the opposite end by the load cell such that the force produced by the robot was entirely supported by the load cell with a factor of the moment arm length ratio. The equipment is shown in Fig. 7.

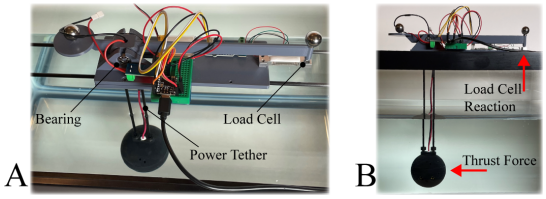

Fig. 7. The propulsion characterization system simultaneously measures robot thrust and power consumption. (**A**) Major components viewed from above. (**B**) Side view depicting the thrust force and load cell reaction.

B. Metrics

1) **Thrust** [mN] defined as the average force generated by a single actuator in steady state operation.
2) **Thrust Density** [mN g^{-1}] defined as the actuator thrust per unit of mechanism mass.
3) **Thrust Cost** [mW mN^{-1}] defined as the total power consumed per unit of actuator thrust.
4) **Cost of Transport** [unitless] defined in the next section, a metric for efficiency of locomotion.

VI. Evaluation

Table II provides a summary of useful propulsion system characterization metrics. These metrics provide a basis of comparison with other propulsion systems operating at a similar scale. The remainder of this section discusses the characterization in more detail.

TABLE II
Propulsion System Characteristics

Mass	9.5 g *
Current Draw at 1 S	0.1 A to 0.9 A *
Thrust	2.3 mN to 74.9 mN *
Thrust Density	0.2 mN/g to 7.9 mN/g
Thrust Cost	41.9 W/N to 159.6 W/N
Estimated Cost of Transport	7.1 to 11.3

*per actuator

A. Thrust Performance

Fig. 8 summarizes data from the thrust characterization. Each actuator produces static thrusts up to 75 mN and consumes 0.4 W to 3.3 W of electrical power. Thrust force and power consumption increase approximately linearly with throttle. The thrust cost decreases with throttle and asymptotically approaches a minimum of 42 mW/mN. Operating regimes near throttles of 60 %, and 80 % experience small increases in thrust cost that correspond to small but sudden increases in power consumption. It is worth noting that these actuators have not been optimized for thrust nor thrust cost. Review of literature shows that the smallest propeller-based mechanisms report significantly less thrust, $\leq$ 40 mN, but with better thrust cost, $\sim$10 Mw/mN [28]. No other propulsion mechanisms have reported comparable thrust or thrust cost at this scale of $\leq$20 mm. Fish-inspired systems do not generally report thrust metrics and will instead be compared by speed and energy metrics.

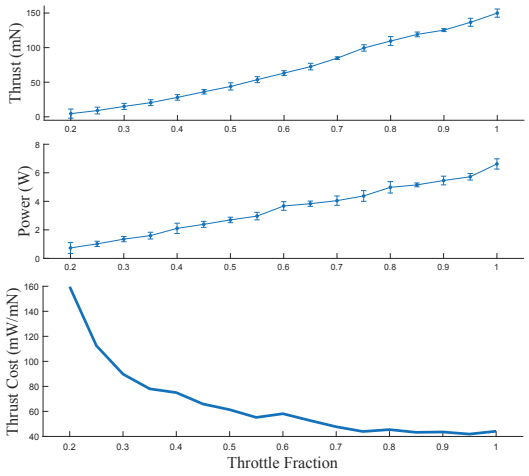

Fig. 8. Data collected from static characterization of the forward actuator pair. Power calculated at a nominal voltage of 3.7 V. Error bars represent standard error ($SE = \sigma/\sqrt{\text{sample size}}$) for eight measurements taken at each data point; for legibility, the thrust and power plots show $10 \times SE$.

B. Motion with Manual Control

A series of motion tests were performed via manual operation of the robot to verify its propulsion system and assess key parameters. Wireless communication was established between a laptop and the robot's microcontroller over Bluetooth Low Energy (BLE), which is only usable for short distances when the robot is at most shallowly submerged. The enclosure was loaded with lead ballast beads to simulate a 15 g payload and the robot was placed in the aquarium tank with an external camera mounted to capture its motion at 60 Hz. A joystick controller was mapped to the robot's propulsion system by the control scheme devised from Fig. 6; for example, pushing the joystick forwards drove the robot forwards. An operator performed a range of motions with the robot at varying thrust levels. Fig. 9 shows some of the trajectories performed. These experiments validated the ability of the propulsion system to drive the robot forwards, to dive, and to rotate in yaw. Speed was measured from video analysis and recorded in Table I. The recorded speeds reflect the maximum values observed from experiments, but do not correspond to the maximum thrust output due to manual control difficulties at actuator throttles greater than $\sim$60 %.

With a continuous forward speed of 250 mm/s, the robot is significantly faster than most fish-like or soft underwater robots in literature [29]. When speed is expressed in terms of vehicle body lengths per second (BL/s), the robot travels at rates comparable to full-size AUV at nearly 4 BL/s [30].

C. Cost of Transport

Cost of transport (COT) is a metric for comparing the energetic cost of motion per unit of mass among different systems. Lower COT indicates higher performance. By convention COT is non-dimensional and measured along directions of motion perpendicular to gravity. This section estimates the robot forward COT by modeling its drag and applying data from its propulsion characterization.

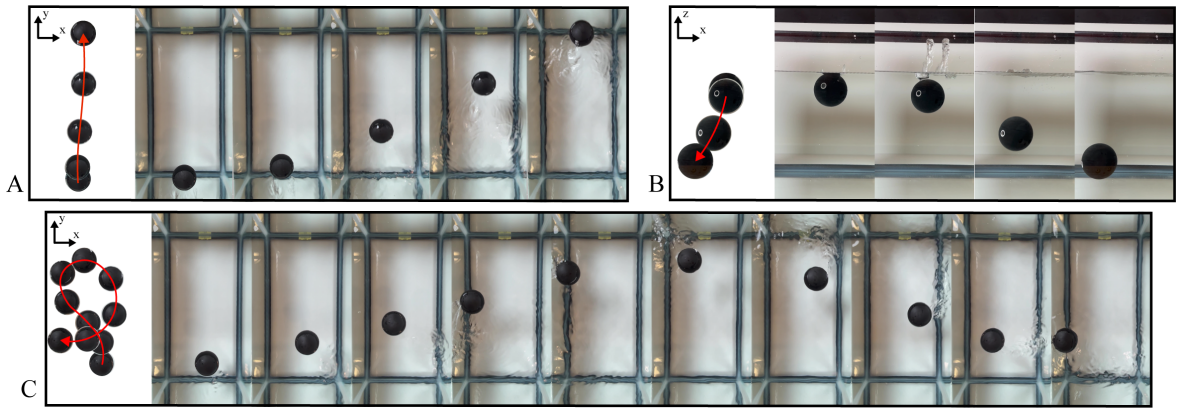

Fig. 9. Examples of motions performed on the robot under teleoperation. Each trajectory begins from rest and is shown by evenly-spaced video frames. Trajectory B is captured from a front-facing camera, and trajectories A, C from an overhead camera. (**A**) Robot drives forwards in a mostly-submerged state with both forward actuators at ∼60 % throttle for ∼2 s. (**B**) Robot dives downwards with both dive actuators at ∼70 % throttle for ∼1 s. (**C**) The robot performs a tight loop in a mostly-submerged state, which involves simultaneous control of forward translation and yaw rate (∼5 s).

The translation drag acting on the robot is approximated by the drag force F_d experienced by an idealized sphere moving through fluid. This system can be evaluated by the canonical drag model [31] from drag coefficient C_d, fluid density ρ, relative fluid velocity u, and reference area A:

$$F_d = \frac{1}{2} C_d \rho u^2 A \tag{6}$$

In constant velocity motion, the total thrust force produced by the propulsion system is equivalent to the drag force that acts on the robot body from (6). It then follows that the COT metric, defined first in its regular form below, can be approximated by two functions, F_e and P_e, that experimentally map the thrust produced and the power consumed by the forward actuators in a characteristic direction. Note that F_e and P_e were experimentally measured and shown by Fig. 8.

$$\text{COT} = \frac{P}{mgu} \approx \frac{P_e}{mg}\sqrt{\frac{C_d \rho A}{2F_e}} \tag{7}$$

This analysis assumes that the dynamic thrust and power consumption of the propulsion system closely matches the static case, and that the exterior of the robot is well-approximated by a sphere. The robot operates at a Reynolds number of $\sim 10^4$ and a corresponding spherical profile drag coefficient of ~ 0.5. The result of applying (7) to the propulsion system characterization is displayed in Fig. 10. The robot is found to have a velocity limit of $6.6\,\text{BL/s}$ or $\sim 400\,\text{mm/s}$. The COT profile generally shows increasing COT with robot velocity, which indicates that the low thrust cost measured at greater throttles does not outweigh the energy lost to increased drag at those greater speeds. The COT profile notably has plateaus and even decreases briefly in the range $4.2\,\text{BL/s}$ to $5.3\,\text{BL/s}$. The robot is estimated to achieve its optimal COT, approximately 7, at speeds less than $160\,\text{mm/s}$. COT generally decreases with increasing mass; smaller systems tend to expend more energy per unit mass to locomote than larger systems. Review of optimal COT among AUV and animals across a large mass range has shown that the COT-mass relationship generally follows a power-law, although

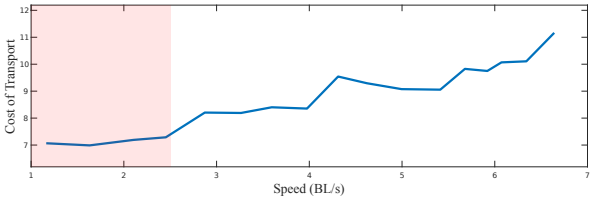

Fig. 10. Estimated robot COT with respect to speed in units of body lengths per second (BL/s), where the robot body length is its diameter (64 mm). The red region indicates an ideal low-COT regime (∼7.1, speed ≤2.5 BL/s)

the parameters vary between AUV and animals, and among different animal swimming mechanics [32]. There is very little literature on μAUV COT at the centimeter scale. One comparable system, the BlueSwarm platform, is reported to have a minimal COT of ~ 8.3 [33]. Biologists have studied many species of fish at this scale and found COT ≤ 1 from metabolic studies [34], but review of swimming robots at the sub-meter scale show machine COT typically ranges between 1 to 100 with larger systems achieving lower COT, and none less than 7 for fully actuated $\sim 100\,\text{g}$ platforms [35] [29].

VII. Conclusion

This research provides steps towards deployable μAUVs at the centimeter scale. The small size of the robot provides access to areas and capabilities previously unreachable by conventional AUVs. The novel jet propulsion system is characterized in detail and shown to have good properties. The robot's modularity, combined with its singular O-ring interface and replaceable shell, offers a durable solution for harsh aquatic environments. The μAUV exhibits good endurance for its scale, but more work is needed to ensure prolonged missions and sufficient autonomy. The next steps of this work include integrating more advanced sensing mechanisms and control, and exploring swarm-based operations.

Acknowledgment

This work is supported in part by the NSF EFRI program (Grant #1830901). The authors are grateful for this support.

REFERENCES

[1] R. B. Wynn, V. A. Huvenne, T. P. Le Bas, B. J. Murton, D. P. Connelly, B. J. Bett, H. A. Ruhl, K. J. Morris, J. Peakall, D. R. Parsons, E. J. Sumner, S. E. Darby, R. M. Dorrell, and J. E. Hunt, "Autonomous underwater vehicles (auvs): Their past, present and future contributions to the advancement of marine geoscience," *Marine Geology*, vol. 352, pp. 451–468, 2014, 50th Anniversary Special Issue. [Online]. Available: https://www.sciencedirect.com/science/article/pii/S0025322714000747

[2] F. Di Ciaccio and S. Troisi, "Monitoring marine environments with autonomous underwater vehicles: A bibliometric analysis," *Results in Engineering*, vol. 9, p. 100205, 2021. [Online]. Available: https://www.sciencedirect.com/science/article/pii/S2590123021000062

[3] A. Gadre, J. Mach, D. Stilwell, and C. Wick, "Design of a prototype miniature autonomous underwater vehicle," in *Proceedings 2003 IEEE/RSJ International Conference on Intelligent Robots and Systems (IROS 2003) (Cat. No.03CH37453)*, vol. 1, 2003, pp. 842–846 vol.1.

[4] A. Underwood and C. Murphy, "Design of a micro-auv for autonomy development and multi-vehicle systems," in *OCEANS 2017 - Aberdeen*, 2017, pp. 1–6.

[5] D. A. Duecker, N. Bauschmann, T. Hansen, E. J. Kreuzer, and R. Seifried, "Hippocampusx – a hydrobatic open-source micro auv for confined environments," *2020 IEEE/OES Autonomous Underwater Vehicles Symposium (AUV)(50043)*, pp. 1–6, 2020. [Online]. Available: https://api.semanticscholar.org/CorpusID:227277895

[6] F. Berlinger, M. Gauci, and R. Nagpal, "Implicit coordination for 3d underwater collective behaviors in a fish-inspired robot swarm," *Science Robotics*, vol. 6, no. 50, 2021, cover Article – Movies – Focus and Science news.

[7] I. C. Rust and H. Harry Asada, "The eyeball rov: Design and control of a spherical underwater vehicle steered by an internal eccentric mass," in *2011 IEEE International Conference on Robotics and Automation*, 2011, pp. 5855–5862.

[8] G. Konidaris, T. Taylor, and J. Hallam, "Hydrogen: Automatically generating self-assembly code for hydron units," 06 2004.

[9] X. Lin, S. Guo, K. Tanaka, and S. Hata, "Development of a spherical underwater robot," in *The 2011 IEEE/ICME International Conference on Complex Medical Engineering*, 2011, pp. 662–665.

[10] S. Bhattacharyya and H. Asada, "Control of a compact, tetherless rov for in-contact inspection of complex underwater structures," in *2014 IEEE/RSJ International Conference on Intelligent Robots and Systems*, 2014, pp. 2265–2272.

[11] Y. Wu, A. Noel, D. D. Kim, K. Youcef-Toumi, and R. Ben-Mansour, "Design of a maneuverable swimming robot for in-pipe missions," in *2015 IEEE/RSJ International Conference on Intelligent Robots and Systems (IROS)*, 2015, pp. 4864–4871.

[12] T. M. Shank, C. Machado, C. R. German, A. Bowen, J. M. Leichty, A. T. Klesh, R. G. Smith, and K. P. Hand, "Development of a New Class of Autonomous Underwater Vehicle (AUV), Orpheus, for the Exploration of Ocean World Analogues," in *Ocean Worlds 4*, ser. LPI Contributions, LPI Editorial Board, Ed., vol. 2168, May 2019, p. 6021.

[13] J. Lee, B. Free, S. Santana, and D. A. Paley, "State-feedback control of an internal rotor for propelling and steering a flexible fish-inspired underwater vehicle," in *2019 American Control Conference (ACC)*, 2019, pp. 2011–2016.

[14] R. Katzschmann, J. DelPreto, R. MacCurdy, and D. Rus, "Exploration of underwater life with an acoustically controlled soft robotic fish," *Science Robotics*, vol. 3, p. eaar3449, 03 2018.

[15] G. Li, X. Chen, F. Zhou, Y. Liang, Y. Xiao, X. Cao, Z. Zhang, M. Zhang, B. Wu, S. Yin, Y. Xu, H. Fan, Z. Chen, W. Song, W. Yang, B. Pan, J. Hou, W. Zou, S. He, X. Yang, G. Mao, Z. Jia, H. Zhou, T. Li, S. Qu, Z. Xu, Z. Huang, Y. Luo, T. Xie, J. Gu, S. Zhu, and W. Yang, "Self-powered soft robot in the mariana trench," *Nature*, vol. 591, no. 7848, pp. 66–71, Mar. 2021.

[16] S. Mintchev, E. Donati, S. Marrazza, and C. Stefanini, "Mechatronic design of a miniature underwater robot for swarm operations," in *2014 IEEE International Conference on Robotics and Automation (ICRA)*, 2014, pp. 2938–2943.

[17] F. Berlinger, J. Dusek, M. Gauci, and R. Nagpal, "Robust maneuverability of a miniature, low-cost underwater robot using multiple fin actuation," *IEEE Robotics and Automation Letters*, vol. 3, no. 1, pp. 140–147, 2018.

[18] J. Jaffe, P. Franks, P. Roberts, D. Mirza, C. Schurgers, R. Kastner, and A. Boch, "A swarm of autonomous miniature underwater robot drifters for exploring submesoscale ocean dynamics," *Nature Communications*, vol. 8, p. 14189, 2017. [Online]. Available: https://doi.org/10.1038/ncomms14189

[19] S. Chen, H. Xu, X. Xiong, and B. Lu, "An underwater jet-propulsion soft robot with high flexibility driven by water hydraulics," in *2023 IEEE International Conference on Robotics and Automation (ICRA)*, 2023, pp. 2613–2619.

[20] Y. Chen, H. Wang, E. F. Helbling, N. T. Jafferis, R. Zufferey, A. Ong, K. Ma, N. Gravish, P. Chirarattananon, M. Kovac, and R. J. Wood, "A biologically inspired, flapping-wing, hybrid aerial-aquatic microrobot," *Science Robotics*, vol. 2, no. 11, p. eaao5619, 2017. [Online]. Available: https://www.science.org/doi/abs/10.1126/scirobotics.aao5619

[21] C. K. Trygstad, X.-T. Nguyen, and N. O. Pérez-Arancibia, "A new 1-mg fast unimorph sma-based actuator for microrobotics," in *2023 IEEE/RSJ International Conference on Intelligent Robots and Systems (IROS)*, 2023, pp. 2693–2700.

[22] S. Schuster, H. Schwanecke, R. D. Dernedde, M. Schmiechen, and H. Schwechheimer, "On certain problems of water jet propulsion," 1962. [Online]. Available: https://api.semanticscholar.org/CorpusID:106665228

[23] N. W. Gladman and G. N. Askew, "The hydrodynamics of jet propulsion swimming in hatchling and juvenile european common cuttlefish, sepia officinalis," *J. Exp. Biol.*, vol. 226, no. 18, Sep. 2023.

[24] K. R. Sutherland and L. P. Madin, "Comparative jet wake structure and swimming performance of salps," *Journal of Experimental Biology*, vol. 213, no. 17, pp. 2967–2975, 09 2010. [Online]. Available: https://doi.org/10.1242/jeb.041962

[25] D. J. Staaf, W. F. Gilly, and M. W. Denny, "Aperture effects in squid jet propulsion," *Journal of Experimental Biology*, Jan. 2014. [Online]. Available: http://dx.doi.org/10.1242/jeb.082271

[26] T. R. Neil and G. N. Askew, "Swimming mechanics and propulsive efficiency in the chambered nautilus," *R. Soc. Open Sci.*, vol. 5, no. 2, p. 170467, Feb. 2018.

[27] O. Chocron and H. Mangel, "Models and simulations for reconfigurable magnetic-coupling thrusters technology," *International Review on Modelling and Simulations*, vol. 4, pp. 325–334, 02 2011.

[28] S. Watson and P. N. Green, "Propulsion systems for micro-autonomous underwater vehicles (μauvs)," *2010 IEEE Conference on Robotics, Automation and Mechatronics*, pp. 435–440, 2010. [Online]. Available: https://api.semanticscholar.org/CorpusID:14054602

[29] J. Qu, Y. Xu, Z. Li, Z. Yu, B. Mao, Y. Wang, Z. Wang, Q. Fan, X. Qian, M. Zhang, M. Xu, B. Liang, H. Liu, X. Wang, X. Wang, and T. Li, "Recent advances on underwater soft robots," *Advanced Intelligent Systems*, vol. 6, no. 2, Oct. 2023. [Online]. Available: http://dx.doi.org/10.1002/aisy.202300299

[30] K. Vasudev, *Review of Autonomous Underwater Vehicles*, 12 2018, pp. 31–34.

[31] R. Flemmer and C. Banks, "On the drag coefficient of a sphere," *Powder Technology*, vol. 48, no. 3, pp. 217–221, 1986. [Online]. Available: https://www.sciencedirect.com/science/article/pii/0032591086800444

[32] A. Phillips, M. Haroutunian, S. Man, A. Murphy, S. Boyd, J. Blake, and G. Griffiths, "Nature in engineering for monitoring the oceans: comparison of the energetic costs of marine animals and auvs," in *Further Advances in Unmanned Marine Vehicles*, ser. 77, G. Roberts and R. Sutton, Eds. The Institution of Engineering and Technology, 2012, pp. 373–405. [Online]. Available: https://eprints.soton.ac.uk/336783/

[33] F. Berlinger, "Blueswarm: 3d self-organization in a fish-inspired robot swarm," PhD thesis, 2021.

[34] J. Videler and B. Nolet, "Costs of swimming measured at optimum speed: Scale effects, differences between swimming styles, taxonomic groups and submerged and surface swimming," *Comparative Biochemistry and Physiology Part A: Physiology*, vol. 97, no. 2, pp. 91–99, 1990. [Online]. Available: https://www.sciencedirect.com/science/article/pii/030096299090155L

[35] R. Baines, S. K. Patiballa, J. Booth, L. Ramirez, T. Sipple, A. Garcia, F. Fish, and R. Kramer-Bottiglio, "Multi-environment robotic transitions through adaptive morphogenesis," *Nature*, vol. 610, no. 7931, p. 283–289, Oct. 2022. [Online]. Available: http://dx.doi.org/10.1038/s41586-022-05188-w